Hybrid model to simulate host cell biomechanics and infection spread during intracellular infection of epithelial monolayers

Raul Aparicio-Yuste [a,b], Lara Hundsdorfer [b], Effie E. Bastounis [b,1], Maria Jose Gomez-Benito [a,*,1]

[a] Multiscale in Mechanical and Biological Engineering (M2BE), Engineering Research Institute of Aragon (I3A), Department of Mechanical Engineering, Universidad de Zaragoza, Zaragoza, 50018, Spain
[b] Interfaculty Institute of Microbiology and Infection Medicine, Cluster of Excellence "Controlling Microbes to Fight Infections" (CMFI, EXC 2124), University of Tuebingen, Tuebingen, 72074, Germany

ARTICLE INFO

ABSTRACT

Mechanical signals are crucial in regulating the response of cells in a monolayer to both physiological and pathological stressors, including intracellular bacterial infections. In particular, during intracellular infection of epithelial cells in monolayer with the food-borne bacterial pathogen *Listeria monocytogenes*, cellular biomechanics dictates the degree of bacterial dissemination across the monolayer. This occurs through a process whereby surrounder uninfected cells mechanically compete and eventually extrude infected cells. However, the plethora of physical mechanisms involved and their temporal dynamics are still not fully uncovered, which could inform whether they benefit or harm the host. To further investigate these mechanisms, we propose a two-dimensional hybrid computational model that combines an agent-based model with a finite element method to simulate the kinematics and dynamics of epithelial cell monolayers in the absence or presence of infection. The model accurately replicated the impact of cell density on the mechanical behaviour of uninfected monolayers, showing that increased cell density reduces cell motility and coordination of motion, cell fluidity and monolayer stresses. Moreover, when simulating the intercellular spread of infection, the model successfully reproduced the mechanical competition between uninfected and infected cells. Infected cells showed a reduction in cell area, while the surrounder cells migrated towards the infection site, exerting increased monolayer stresses, consistent with our *in vitro* observations. This model offers a powerful tool for studying epithelial monolayers in health and disease, by providing *in silico* predictions of cell shapes, kinematics and dynamics that can then be tested experimentally.

1. Introduction

Cells sense and respond to mechanical cues that arise both intrinsically, from their own internal structures (e.g., actomyosin force generation), and externally, from their microenvironment (e.g., fluid shear stresses) [1–4]. Recent studies on interactions of host cells with bacterial pathogens, have proven that mechanical forces play a key role in both driving bacterial spread and aiding the host cells to get rid of the infection [5–9]. These seminal works showcase that understanding how bacteria alter the properties of host cells or how host cells dynamically respond to the presence of pathogens is crucial, if we were to develop strategies alternative to antibiotics for combating bacterial spread and dissemination [10].

In our previous *in vitro* studies, we discovered a mechanism that limits intracellular bacterial dissemination through epithelial cells (ECs) in monolayer. We showed that a mechanical competition arises during infection of ECs with food-borne bacterial pathogen *Listeria monocytogenes* (*L.m.*), whereby softer and less contractile infected cells get squeezed and extruded by the action of stiffer and more contractile uninfected surrounding cells, which collectively migrate towards the site of infection [11,12]. We found that this process leads to the death of extruded infected cells and also occurs during infection with other intracellular pathogens that similar to *L.m.*, use actin comet tails to spread from cell to cell [11]. The intestinal epithelium is the primary site of infection of enteropathogens like *L.m.*, and is thereby the first barrier bacteria have to overcome to spread to secondary sites, with often fatal consequences [13]. Therefore, it is of particular interest to understand how bacteria establish infection there and how the ECs of the intestinal lining manage to obstruct their dissemination [13].

Studying the mechanobiology of the interactions between intestinal ECs and *L.m. in vivo* is currently very challenging, thus *in vitro* models

---

* Corresponding author.
  E-mail addresses: effie.bastounis@uni-tuebingen.de (E.E. Bastounis), gomezmj@unizar.es (M.J. Gomez-Benito).
[1] Co-senior authors, contributed equally.

like organoids or gut-on-chips that can mimic the structure of the intestine to some extent [14,15] are increasingly used. However, under such settings (three-dimensional, 3-D), monitoring the infection process with live-cell imaging and concurrently characterizing host cell mechanics is still challenging. Therefore, biomechanical interactions between host cells and pathogens are usually investigated *in vitro* using two-dimensional (2-D) epithelial monolayers. Under these conditions, for example, one can use live cell imaging, combined with cell segmentation and tracking, or alternatively, particle image velocimetry (PIV) to analyse in detail cell motion, including properties such as directionality and coordination of motion over different scales [16,17]. The dynamics that lead to the alterations in cell kinematics can also be calculated. For instance, techniques such as traction force microscopy (TFM) allow calculating the traction stresses that cells exert on their matrix, a proxy for how well the cytoskeleton is organised and connected to the extracellular matrix (ECM) through adhesion complexes [2,5]. Additionally, techniques like monolayer stress microscopy allow inferring intra- and inter-cellular stresses [18–20]. All these techniques can reveal alterations that occur during (patho)physiological processes, including infections. But they can also provide critical input data to build accurate computational models to predict cell behaviour *in silico*.

These computational models have proven to be powerful tools that complement *in vitro* studies, offering often unique and new insights into infection mechanobiology [6,11]. However most of the published models primarily focus on simulating the formation of bacterial biofilms and the forces implicated therein [21–23], or on the growth of microcolonies such as those of bacteria like *Escherichia coli* [24]. These types of models generally take into account bacterial proliferation, interaction forces between bacteria, and friction forces between the bacteria and their substrate, but not interactions of bacteria with host cells [25]. While agent-based models have been developed to simulate the intracellular motion of bacteria modelled as single particles moving within host cells [26], very few studies have so far focused on developing models to simulate interactions of bacteria like *L.m.* with host cells in monolayer [6,11]. These models enable the exploration of the impact of geometrical properties (e.g., cell area or polarization), mechanical properties (e.g., cell stiffness), and the contribution of cellular forces (e.g., stress distribution in the monolayer) on the outcome of the infection process. For example, in our previously developed 3-D *in silico* model we were able to simulate the mechanical competition between *L.m.*-infected and surrounding uninfected cells [11]. This model was constructed using a continuum approach, a finite element model. In a follow-up study, where we additionally considered the stiffness of the ECM where cells reside, we were able to predict that collective extrusion of infected cells would be exacerbated on stiffer ECMs, which was then confirmed experimentally [12]. However, our model did not account for infection spread as it was not designed to simulate long time scales. Furthermore, we assumed an idealised hexagonal geometry for epithelial cells. Because changes in cell shape and propagation of bacterial infection are key in understanding infection processes, there is a need for more sophisticated models that can account for these parameters as well.

To fill this gap, we introduce here a 2-D computational hybrid model to study the modulation of host cell shape, motion and forces during infection with intracellular *L.m.* In this model we also account for infection spread dynamics. To that end, we combined a discrete with a continuum model by integrating an agent-based model (ABM) with a finite element method (FEM), to concurrently simulate the mechanics and geometry of cell epithelial monolayers. We first calibrated and validated our *in silico* model by examining *in vitro* the behaviour of uninfected cell monolayers via videomicroscopy. We then confirmed that the hybrid model successfully represents the kinematics and dynamics of uninfected cell monolayers, thereby validating our mechanical approach. The model accurately replicated the impact of cell density on the mechanical behaviour of uninfected monolayers, demonstrating that increased cell density reduces cell motility and coordination of

motion, cell fluidity and monolayer stresses. Finally, we accounted for infection spread within our *in silico* cell monolayers. When simulating the intercellular spread of infection, the model successfully reproduced the mechanical competition that arises between uninfected and infected cells *in vitro*. Infected cells showed a reduction in cell area, while the surrounder cells migrated towards the infection site, exerting increased monolayer stresses, consistent with our *in vitro* observations.

2. Materials and methods

Our hybrid model combines two different modelling approaches: discrete and continuum [27,28]. Discrete models represent cells as particles, considering the individual properties of cells and their inherent spatial irregularities [29–31]. In contrast, continuum models are based on macroscopic properties and are defined by constitutive laws [32–34]. To overcome the inherent limitations of either aforementioned model, we combine a discrete with a continuum model by integrating an Agent-Based Model (ABM) with a Finite Element Method (FEM) respectively, to simulate the mechanics and geometry of cell epithelial monolayers. The integration of the ABM and FEM enables us to model the tissue as a continuum medium, capturing its collective mechanical behaviour while also considering the heterogeneity and interactions acting at the cellular level. Leveraging previous work [35], we propose a new hybrid model that takes into account changes in the mechanical behaviour of infected and non-infected cells, and the mechanical battle between the two cell populations that leads to the formation of collectives of infected squeezed and subsequently extruded cells (infection mounds).

2.1. Discrete approach

In our hybrid computational model, we take advantage of the ABM approach to simulate both the geometry of the epithelial cell monolayer and changes in cellular forces. To do so, we choose a centre-based approach for EC in 2-D, meaning that cells are represented by their central point or centroid (see cell centroid positions, Fig. 1). Thus, ECs are accounted as individual non-deformable particles that move independently and interact with other neighbouring cells by sensing mechanical inputs [31,36]. Each cell has unique properties and is defined as a singular entity as $C_i(\mathbf{x}_i)$, where $\mathbf{x}_i$ is the position of the i_{th} cell centroid in the cell monolayer. In the ABM, each particle is associated with a virtual radius R_i, which defines the range within which a particle can interact with other particles. The set of cells is denoted as defined in Eq. (1):

$$\mathbf{C} = \{C_1, C_2, \dots, C_n\} \tag{1}$$

being n the total number of cells. To generate the cell shape, we approximate the cell geometry by making use of the Voronoi diagram to associate a polygon V_i to each cell C_i in the monolayer, as defined in Eq. (2):

$$V_i = \{\mathbf{x} \in \mathbb{R}^2 : d(\mathbf{x}, \mathbf{x}_i) < d(\mathbf{x}, \mathbf{x}_j) \, for \, i \neq j\} \tag{2}$$

where $d(\mathbf{x}, \mathbf{x}_i)$ is the distance between a point $\mathbf{x}$ and the cell centroid $\mathbf{x}_i$ of the cell C_i. The polygon V_i includes all the points that are closer to the cell centroid of C_i than to any other cell C_j. The Voronoi diagram allows the division of the plane in different regions and is an approximation of the cell shape [37] (see Voronoi diagram and polygon labelling, Fig. 1).

Cell motion requires forces of different nature generated and transmitted through the cell cytoskeleton to the cell matrix or to neighbouring cells. E.g., the actomyosin apparatus allows cells to contract or transmit forces to their surrounding while microtubules allow cells to resist large-scale compressive forces exerted onto them [38,39]. Thus, cell shape results from the contribution of various forces exerted within the cell and by its surroundings (i.e., surrounding cells or extracellular
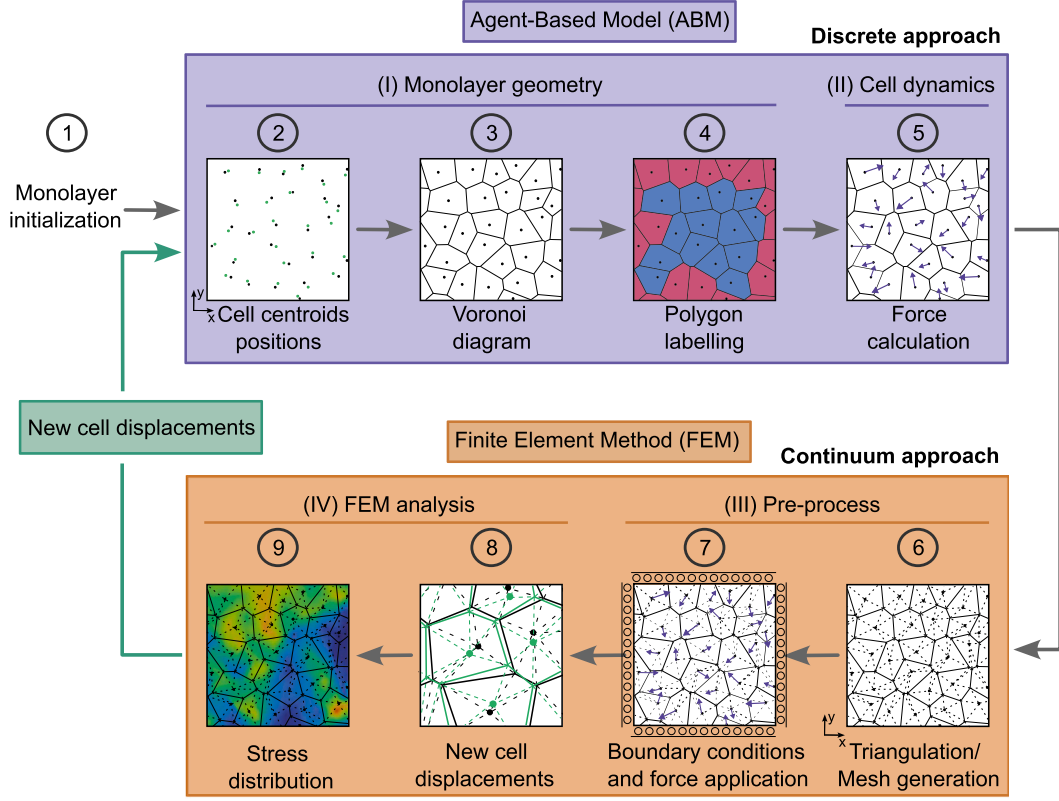
Fig. 1. 2-D Hybrid computational model of cell epithelial monolayers. Schematic illustration showing the iterative loop of the hybrid model (discrete approach in purple, continuum approach in orange). The monolayer is initialised (step 1), resulting in a distribution of cell centroids (black points; step 2). Those serve as inputs to compute the Voronoi diagram (step 3), providing a distribution of polygons (exterior cells in red and interior cells in blue; step 4). Afterwards, cell forces are computed (step 5). Once the monolayer geometry and forces are defined, a continuum mesh is generated through the triangulation of each cell polygon (step 6). Additionally, both boundary conditions and the forces previously computed in the ABM are applied to the monolayer (step 7). These forces induce deformations in the monolayer, causing the movement of cells (new cell displacements in green; step 8). Secondary variables are also computed (e.g., monolayer stresses; step 9). To close the iteration loop, we retrieve the new cell centroid displacements from step 8 and update the distribution of cell centroids (green points in step 2).

environment). We assume balance of cellular forces since inertial terms are negligible and cells are under quasistatic equilibrium within an epithelium [40]. Thus, the force balance for each cell is defined in Eq. (3):

$$\sum_j \mathbf{F}_i^j = m_i \cdot \frac{d\mathbf{v}_i}{dt} \rightarrow \sum_j \mathbf{F}_i^j = 0 \tag{3}$$

where $\sum \mathbf{F}_i^j$ is the total force at the cell centroid, m_i the mass of the i_{th} cell and $\mathbf{v}_i$ its velocity. The total force for each cell (see Force calculation, Fig. 1) is calculated as the sum of all cell forces due to cell–cell interaction forces $\mathbf{F}_i^{cell-cell}$, cell contraction forces $\mathbf{F}_i^{contr}$, cell protrusion forces $\mathbf{F}_i^{protr}$ and surrounder cell forces $\mathbf{F}_i^s$, as defined in Eq. (4):

$$\sum_j \mathbf{F}_i^j = \mathbf{F}_i^{cell-cell} + \mathbf{F}_i^{contr} + \mathbf{F}_i^{protr} + \mathbf{F}_i^s = 0 \tag{4}$$

Cell–cell interactions ($F_{ji}^{cell-cell}$)

The junctional network and cell–cell adhesion molecules connect the cell cytoskeleton to neighbouring cells, enabling cells to exert forces onto each other [41]. We model these cell–cell mechanical interactions by using a force-derived formulation from the Lennard-Jones potential [42], as defined in Eq. (5):

$$F_{ji}^{cell-cell} = -12 \cdot K^{cell-cell} \cdot \left[\frac{d_m^{12}}{d^{13}} - \frac{d_m^6}{d^7}\right] \tag{5}$$

where $F_{ji}^{cell-cell}$ is the force interaction between the adjacent j_{th} cell with the i_{th} cell, $K^{cell-cell}$ is the cell–cell interaction constant, d_m is the equilibrium distance and d is the distance between the centroids of the neighbouring cells. Under this formulation, the force interaction between neighbouring cells has two main contributions: (1) the

attractive d_m^{12}/d^{13} and (2) repulsive d_m^6/d^7 terms. The attractive term represents intercellular cohesive forces acting as two cells are pulled apart, whereas the repulsive term accounts for the repulsion that occurs when two cells are in close proximity. The distance d_m is the distance where the Lennard potential is minimum and is equal to the sum of the virtual radius of each cell ($d_m = R_i + R_j$). The direction of the force is defined by the vector that joins the centre of mass of the adjacent j_{th} cell with the respective i_{th} cell (see cell–cell interactions, Fig. 2). The resultant force for the i_{th} cell is defined in Eq. (6):

$$\mathbf{F}_i^{cell-cell} = \sum_{j=1}^m \mathbf{F}_{ji}^{cell-cell} \tag{6}$$

being m the total number of neighbouring cells of the i_{th} cell.

Actomyosin contraction ($F_{k,i}^{contr}$) and cell protrusion ($F_{k,i}^{protr}$) forces

Epithelial cell movement directly depends on the action of the actomyosin contractile apparatus (actomyosin contraction forces) and on the actin polymerization machinery resulting in forces for cell protrusion (cell protrusion forces) and movement [43,44]. Instead of modelling cell motion in epithelial monolayers as a random stochastic phenomenon, we propose here a contraction and protrusion law that depends on the mechanical stress distribution that each individual cell is experiencing. We consider a cell mechanotransduction mechanism that generates a heterogeneous force distribution in the monolayer, leading to the movement of cells within the epithelial monolayer according to their mechanical state [45]. This new contraction and protrusion law defines the level of cell contraction or protrusion depending on the principal stress distribution within the cell, which is provided by the continuum model. We assume the contraction and protrusion

forces are proportional to the maximum averaged tensile stress the cell is subjected to. These contraction and protrusion forces are applied on the cell vertex (see actomyosin contraction and cell protrusion forces, Fig. 2). The average cell stress tensor $\overline{\sigma}(\boldsymbol{x}_i)$ in the whole cell is defined in Eq. (7):

$$\overline{\sigma}(\boldsymbol{x}_i) = \frac{\int_{A_i} \sigma \, dA}{A_i} \tag{7}$$

where A_i represents the area of the cell and σ the stress tensor associated to each infinitesimal cell area. From this stress tensor, we compute its principal values to obtain the maximum averaged principal tensile stress of the cell $\overline{\sigma}_I$. According to our proposed contraction law, the magnitude of the contraction force $F_{k,i}^{cont}$ in each cell vertex k is defined in Eq. (8):

$$F_{k,i}^{cont} = K^{cont} \cdot A_i \cdot \overline{\sigma}_I \cdot \left(\frac{l_{k,i}^R + l_{k,i}^L}{2 \cdot P_i} \right) \tag{8}$$

where K^{cont} is the contraction constant and the term in brackets defines a length ratio, being equal to the sum of the half-lengths of the edges that meet at the k vertex (i.e., the right $l_{k,i}^R$ and left $l_{k,i}^L$ edges), divided by the total perimeter P_i of the cell [46] (see actomyosin contraction, Fig. 2). The direction of the contraction force is defined by the vector that joins the cell vertex to the cell centroid. According to Newton's third law (action–reaction), an equal magnitude and opposite direction force is applied to the cell centroid (actomyosin contraction, Fig. 2). Thus, the total contraction force in the cell centroid for the i_{th} cell is defined in Eq. (9):

$$\mathbf{F}_i^{contr} = \sum_{k=1}^m \mathbf{F}_{k,i}^{cont} \tag{9}$$

m being the total number of vertices associated to the i_{th} cell. Similarly, according to our proposed protrusion law [45], the magnitude of the protrusion force $F_{k,i}^{protr}$ in each vertex k results in Eq. (10):

$$F_{k,i}^{protr} = K^{protr} \cdot A_i \cdot \overline{\sigma}_I \cdot \left(\frac{l_{k,i}^R + l_{k,i}^L}{2 \cdot P_i} \right) \tag{10}$$

where K^{protr} is the protrusion constant. The force direction is determined by the vector connecting the cell vertex to its centroid, with an equal and opposite force applied at the cell centroid. The total protrusion force exerted to the i_{th} cell centroid results in Eq. (11):

$$\mathbf{F}_i^{protr} = \sum_k \mathbf{F}_{k,i}^{protr} \tag{11}$$

where we assume the cell protrudes towards the direction of minimal $\overline{\sigma}_I$, thereby affecting the k vertices of the cell that are nearest to this direction.

Surrounder cell forces (F^s)

Surrounding uninfected cells migrate actively towards the *L.m.* infection focus leading to the formation of infection mounds (collectives of infected squeezed and extruded cells). These mounds result from the mechanical competition between surrounder cells and infected cells, where the former are stiffer and more contractile than the latter [11, 12]. To consider the modulation of forces during the competition between infected and uninfected surrounder cells, we additionally include uninfected surrounder cell forces in our model (surrounder cell forces, Fig. 2). The infection force magnitude in each vertex k is assumed to be proportional to the surrounder constant K^s and the length ratio, as defined in Eq. (12):

$$F_{k,i}^s = K^s \cdot \frac{l_{k,i}^R + l_{k,i}^L}{P_i} \tag{12}$$

These forces are only applied to the vertices of the uninfected surrounder cells that are at the border of the infection focus (also referred to as immediate surrounder cells). By infection focus we refer to the domain comprising infected cells [6,11]. In our model, we reproduce the infection spread of *L.m.*, which leads to an increase of the infection

focus area. Following Newton's third law of action and reaction, we also apply an equal magnitude and opposite direction force to the cell centroid, being this one the force we illustrate (surrounder forces, Fig. 2). The resultant force acting at the i_{th} cell centroid is defined in Eq. (13):

$$\mathbf{F}_i^s = \sum_k \mathbf{F}_{k,i}^s \tag{13}$$

where k represents the cell vertices that are at the border of the infection focus.

2.2. Continuum approach

After implementing cells as individual entities in the ABM, we make use of a continuum approach to account for the collective mechanical behaviour of cells [47]. Under this assumption, cells no longer exhibit particle-like behaviour, instead, they are considered as a 2-D deformable body whose mechanical properties rely on macroscopic equations [27]. Under the context of Solid Mechanics, cells within the monolayer must satisfy the internal equilibrium equation, defined in Eq. (14):

$$\nabla \sigma + \mathbf{f} = 0 \tag{14}$$

where σ is the stress tensor and $\mathbf{f}$ the volumetric forces. This equation is solved here through a FEM, considering the cell epithelial monolayer as an elastic structural material under the assumption of the plane-stress problem. The forces previously computed in the ABM are applied in the FEM, inducing deformations in the monolayer, eventually causing the movement of cells (see FEM in Fig. 1). For a more detailed explanation of the implementation of the model, please refer to the Supplementary Information (S1.1 Implementation of the hybrid model). Sample input images for each step of the hybrid model, along with the workflow of the model for simulating epithelial cell monolayers, are shown in Supplementary Figure S1.

2.3. In vitro experiments

To validate our model, we performed experiments with Madin-Darby Canine Kidney (MDCK) epithelial cells to characterise the kinematics, morphometrics and dynamics of both uninfected and infected MDCK epithelial monolayers. To achieve that, we first constructed polyacrylamide hydrogels with fluorescent beads, and then we seeded MDCK cells on these hydrogels. In the case of infection, MDCK monolayers were exposed to *L.m.* We then imaged MDCK cells to analyse cell kinematics, cell shape changes and cell dynamics (Traction Force Microscopy and Monolayer Stress Microscopy). For more detailed information about our *in vitro* experiments, please refer to the Supplementary Information (S1.2 *In vitro* experiments for characterization of kinematics, morphometrics and dynamics of uninfected and infected MDCK epithelial cell monolayers). The experimental data used for validating the hybrid model are presented in Supplementary Figure S2A, and the data analyses performed are shown in Supplementary Figure S2B.

3. Results

We initially validated our *in silico* model using uninfected monolayers under two different cell density conditions: low and high. We examined the evolution of cell shape, cell motility, coordination of cell movement, and the forces exerted between cells, analysing these factors across both our simulations and *in vitro* experiments. After validating our model with the *in vitro* results, we incorporated the modulation of infection forces and infection spread into our hybrid *in silico* model, specifically assuming the scenario of a high cell density monolayer. We then analysed infection spread, the geometrical properties of cells, and their coordination in both *in vitro* and *in silico* models. Furthermore, we conducted a further analysis of the stress distribution among cells during the mechanical competition arising upon *L.m.* infection.
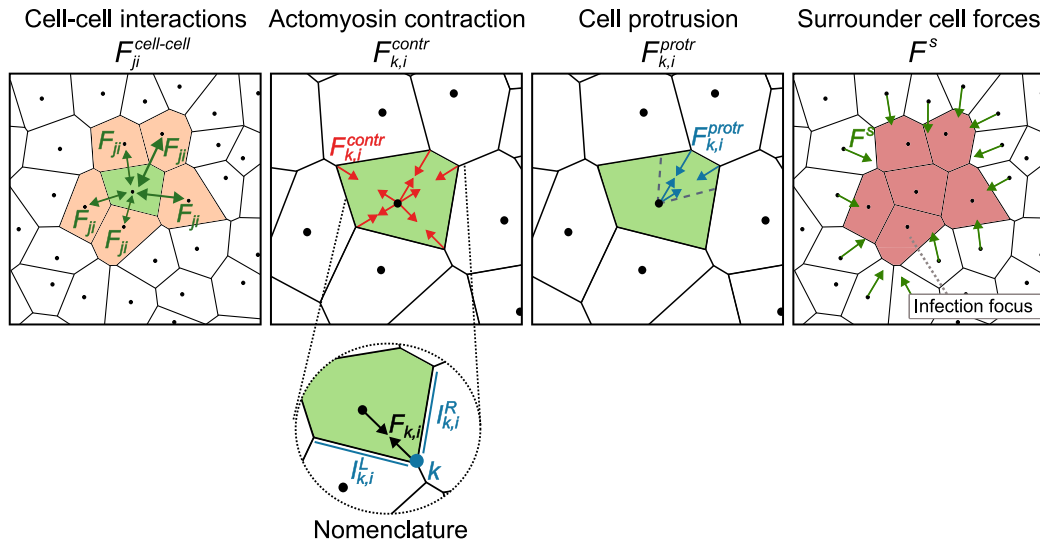
Fig. 2. Cell forces considered in the hybrid model. $F_{ji}^{cell-cell}$ represents the interactions between the i_{th} cell (in green) and its neighbours (in orange). $F_{k,i}^{contr}$ denotes the actomyosin contraction forces, with i_{th} indicating the respective cell (in green) and k representing a given vertex of the cell. The nomenclature (inset) shows the terms defined in Eq. (8), depicting the edges associated with the k vertex: the left ($l_{k,i}^{L}$) and right ($l_{k,i}^{R}$) edges. $F_{k,i}^{protr}$ represents the protrusion forces of the i_{th} cell at their k vertices. These forces are applied only in the direction of protrusion. F_s symbolises the surrounder cell forces, accounting for the migration of immediate neighbouring uninfected cells (in white) towards the infection focus composed by infected cells (in pink).

3.1. In silico model predicts how cell density regulates shape of epithelial cells in monolayer

The organization and shape of ECs in monolayer are known to be dependent on physical factors such as cell density [48]. To explicitly investigate the role of cell density in regulating cell shape and to validate our computational model, we first performed experiments on uninfected MDCK monolayers, and used the resulting *in vitro* data to validate our model. Specifically, time-lapse multichannel epifluorescence microscopy was used to monitor monolayers of MDCK cells residing on 3 kPa collagen-I coated hydrogels over the course of 23 h. The hydrogels were embedded with fluorescent tracer beads to allow concurrent performance of traction force microscopy, and thus characterise both the kinematics and dynamics of cells (see Sections 3.2 and 3.3) [49,50].

At each instance of time we acquired the following images: (1) the phase contrast image of cells; (2) the nuclei fluorescence of cells; and (3) the image of fluorescent tracer beads (Supplementary Figure S2). We used both the phase contrast image and the nuclei fluorescence to automatically segment and track the cells overtime using the Track-Mate and Cellpose detector plugins in Fiji (Supplementary Video S1) [51–53]. Since cell density in our monolayer at the beginning of the recordings was relatively low, cells proliferated over the course of the recordings reaching maximum packing density at approximately 20 h. (Supplementary Video S2). We thus selected one of the first frames (cells at low density, $\rho = 2377$ cells/mm^2) and one of the last frames (cells at high density, $\rho = 5786$ cells/mm^2), to compute the geometrical parameters associated with the shape of cells in monolayer as a function of their density (Fig. 3A, *in vitro* segmentation). We found that as cell density approximately doubles, cell area decreases by 62% and cell perimeter by 43% (Fig. 3A,C *in vitro* and Supplementary Figure S3 *in vitro*). *In vitro*, the average cell area was found to be 445 and 169 μm^2 for low and high cell densities, respectively, and the average cell perimeter was 90 and 51 μm for low and high cell densities, respectively.

To test our model, we simulated the behaviour of cells in monolayer under conditions not involving infection and considering two different cell densities, namely, low cell density ($\rho = 2390$ cells/mm^2) and high cell density ($\rho = 5708$ cells/mm^2), mimicking the initial and final cell densities in our *in vitro* experiments, respectively (Supplementary Video S3 and S4). Note that in both cases, cell confluence is 100%,

meaning there is no void space and cells occupy the whole area considered, similar to our *in vitro* condition. Consistent with previous findings [48], we assumed that cell spatial distribution is influenced by how densely populated the monolayer is. In accordance to the experimental results, our model showed that as cell density increases, the average cell area and perimeter decrease from 418 to 175 μm^2 and 79 to 50 μm, respectively (Fig. 3A,C *in silico* and Supplementary Figure S3). Moreover, we were able to validate the geometric distribution of cells in the monolayer since we achieved similar values in both area and cell perimeter as in the *in vitro* experiments (Fig. 3C and Supplementary Figure S3). In our simulations, as cell density approximately doubles, cell area decreases by 58% and cell perimeter by 37%.

In previous work, the cell shape index (CSI), equal to the perimeter of cells divided by the square root of their area, has been used to characterise cellular fluidity and anisotropy [54,55]. Typically, solid-like cells exhibit a CSI lower than 3.813: the higher the value of the CSI the more fluid-like and anisotropic cells become [55,56]. We thus wondered if and how density of MDCK cells in monolayer would impact CSI *in vitro* and *in silico*. We found that in our *in vitro* experiments, cells at low density exhibit an averaged CSI equal to 4.39. As cell density doubles, the average CSI becomes significantly lower and equal to 4 (Fig. 3B,C). This finding suggests that at higher cell density cells become more solid-like as would be expected [57]. We then calculated the average CSI for our *in silico* model. At low cell density, the average CSI in our model is equal to 3.9. As cell density increases twofold, the average CSI becomes equal to 3.7 (Fig. 3C).

To recapitulate both *in vitro* and *in silico* we observed that doubling density of ECs in monolayer decreases their area approximately by 60%, their perimeter by 40% and their fluidity (9% *in vitro* and 5% *in silico*). The results related to the geometry of the monolayer are summarized in Table 1.

3.2. Increasing density of epithelial cells in monolayer leads to reduction of cell motility speed and coordination in vitro and in silico

Doubling the density of ECs in monolayer is expected to lead to a reduction in cell motility [17]. To discover to which extent cell density leads to a reduction in cell motility, and whether a reduction in motility impacts in any way the coordination of motion between neighbouring ECs, we tracked individual cells using Track-Mate and
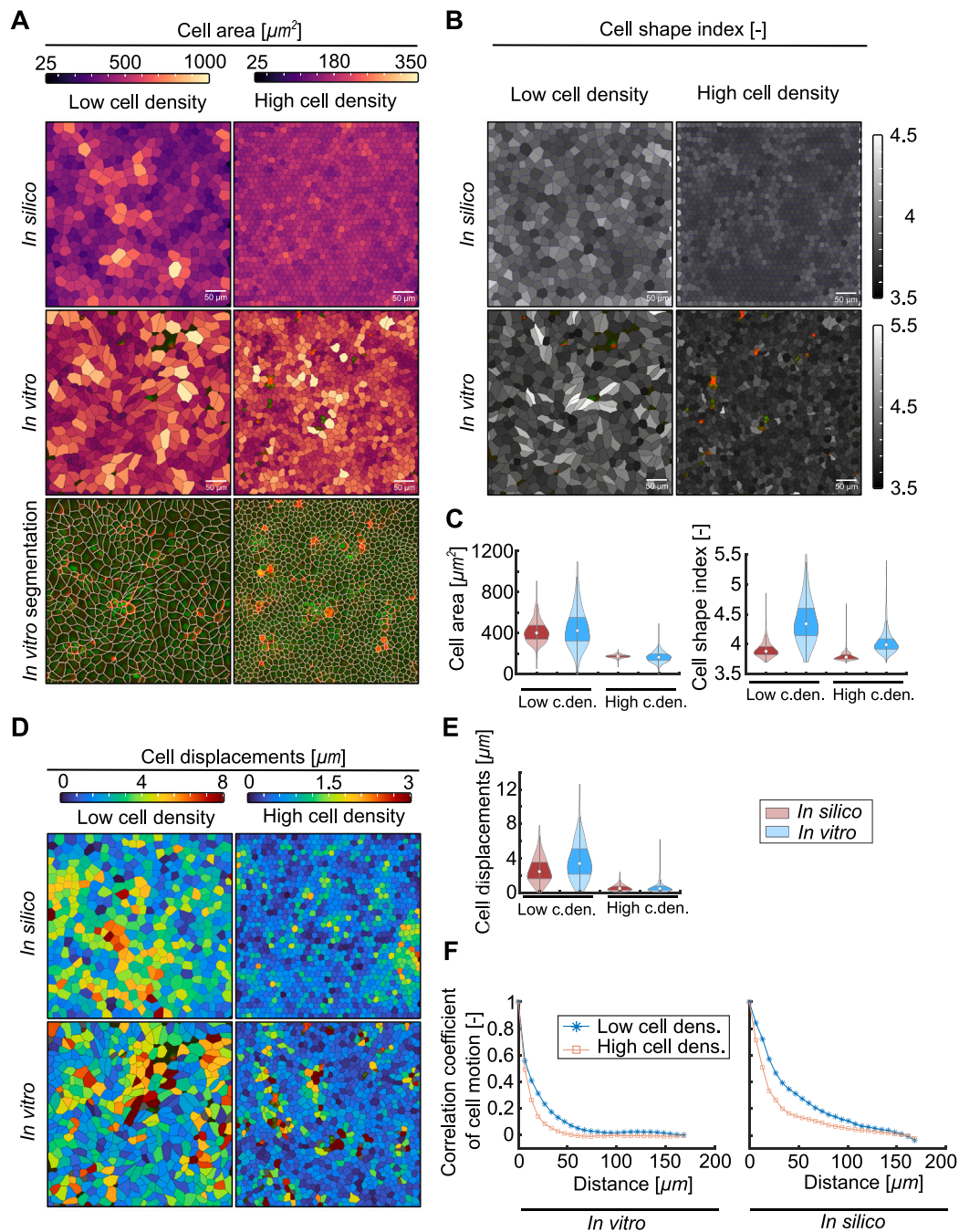
Fig. 3. Increased cell density alters the shape of epithelial cells and reduces their motility and coordination in both *in vitro* and *in silico* models (A) Map of cell area with varying cell densities. Note that the colour bars differ between low and high cell densities (first and second columns, respectively). Rows display: *in silico* and *in vitro* cell areas, and the automatic *in vitro* segmentation of cells. Note that some areas were not accurately segmented. (B) Similar to panel A, but the images depict the cell shape index. (C) Violin plots of cell area (left column) and cell shape index (right column) associated with the frames shown in panels A and B. (D) Map of cell displacements at low and high cell densities in both *in silico* and *in vitro* models. Note the different colour bars for each cell density. (E) Violin plots showing the distribution of cell displacements shown in panel D. (F) Plots demonstrating the correlation coefficient of cell displacement vectors as a function of distance in both *in vitro* (left) and *in silico* (right) models for each cell density.

Cellpose detector plugins in Fiji, and also performed particle image velocimetry (PIV) on the phase contrast image of cells to compute their correlation coefficient [58] (Supplementary Figure S2). Using these orthogonal approaches, we found that as cell density approximately doubles (from 2390 to 5708 cells/mm²), cell motility speed decreases by approximately 80% (Fig. 3D,E *in vitro*). The average cell displacements were found to be 3.65 and 0.72 μm for low and high cell densities, respectively. We then calibrated our *in silico* model to obtain cell displacements of similar magnitude based on cell density (Fig. 3D,E *in silico*). Our *in silico* average cell displacements were found

to be 2.65 and 0.55 μm for low and high cell densities, respectively. Additionally, using the displacements of cells resulting from the PIV analysis, we calculated the degree of correlation of neighbouring displacement vectors as a function of the distance [17]. We found both *in vitro* and *in silico* that the correlation coefficient decays faster over distance in higher density conditions (1.81 times faster *in vitro* and 1.66 times faster *in silico*), suggesting that cells exhibit greater coordination in their movement over larger distances when cell density is lower (Fig. 3F). Note though, that the correlation coefficients we obtained *in silico* at both densities are slightly higher than the ones calculated
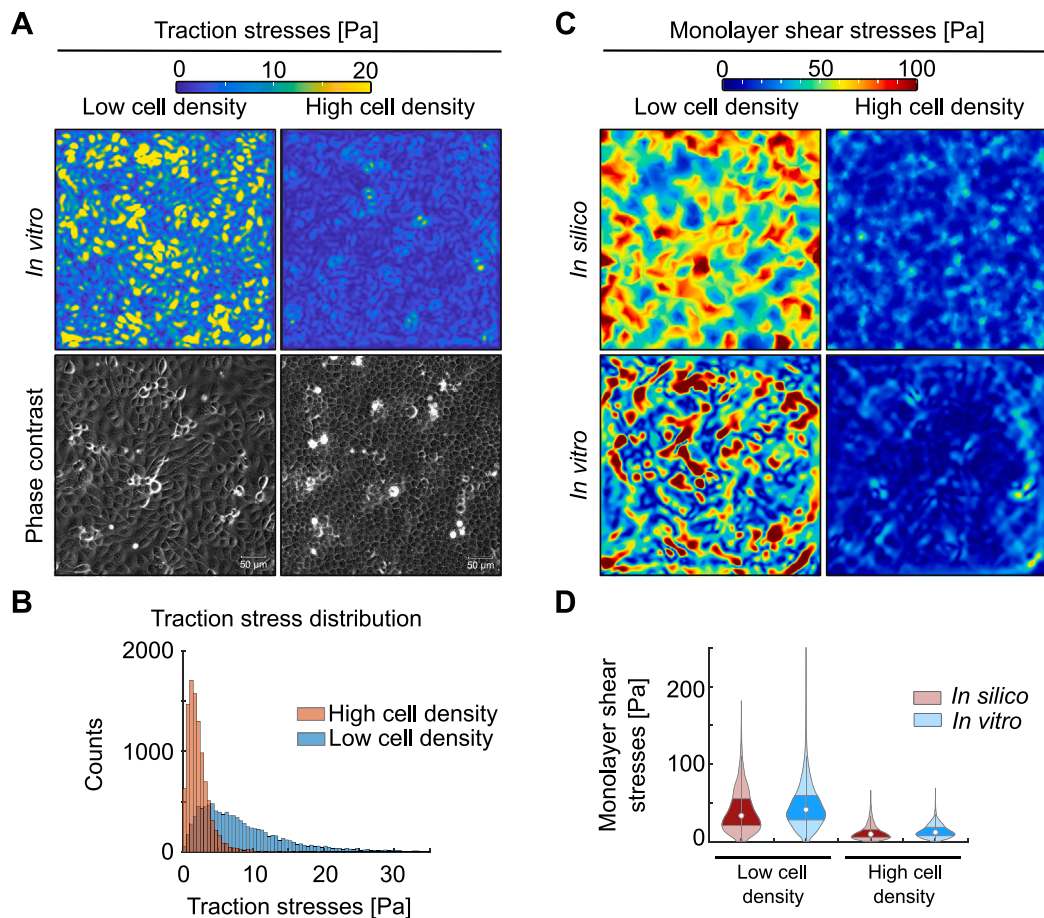
Fig. 4. **Higher epithelial cell densities reduce traction forces *in vitro* and decrease monolayer stresses both *in vitro* and *in silico*.** (A) Map of traction stresses at low and high cell density (left and right column, respectively). Rows display *in vitro* traction stresses and phase contrast images of MDCK epithelial monolayers. *In silico* traction stresses are not shown, as our hybrid model do not simulate the ECM. (B) Histograms of traction stresses for both cell densities shown in panel A. (C) Map of monolayer shear stresses at low and high cell densities (left and right columns, respectively). (D) Violin plots of monolayer shear stresses corresponding to the frames shown in panel C.

in vitro. Nevertheless, the trends are similar and both *in vitro* and *in silico* we found that increasing cell density reduces cell migration speed and coordination of motion. The results related to the kinematics of the monolayer are summarized in Table 1.

3.3. Increasing epithelial cell density weakens monolayer stresses both in vitro and in silico

Our experimental and computational findings demonstrate that the geometrical properties and kinematics of ECs in monolayer are heavily dependent on cell density. Accordingly, one would expect that EC dynamics should also vary based on cell density. To test that *in vitro*, we measured the traction stresses that cells exert on a 3 kPa matrix on which they reside, as a function of cell density, using TFM. We found that as cell density doubles, mean traction stresses decrease by 74% consistent with previous studies [59](Fig. 4A and Table 1). Interestingly, we also observed the traction stress distribution to be modified, showing a narrower distribution and a higher peak under conditions of high cell density as compared to low cell density (Fig. 4B). This suggests that the traction stresses at high cell density are more homogeneous than at low density. We then performed monolayer stress microscopy (MSM) to compute the monolayer stresses of ECs (i.e., intra- and inter-cellular stresses) [18,20]. We discovered that as cell density approximately doubles (2.4 fold higher), monolayer shear and tensile stresses decrease by 3.36-fold (Fig. 4C,D *in vitro* and Supplementary Figure S4). The average monolayer shear stresses were 46.7 and 13.9 MPa for low and high cell densities, respectively, whereas the average tensile stresses were 46.52 and 13.82 MPa, respectively (Table 1).

To assess how our model predicts this density-dependent dynamic behaviour of cells, we analysed the monolayer stresses in uninfected monolayers of different cell densities *in silico*. Through our simulations we discovered that monolayer shear and tensile stresses increase with decreasing cell density to the same extent as *in vitro* (Fig. 4C,D and Supplementary Figure S4). The average monolayer shear stresses in our simulations decreased from 40.17 to 12.46 MPa as cell density doubled, whereas the average tensile stresses from 47.36 to 13.68 MPa. Thus, our *in silico* model is able to successfully replicate the *in vitro* dynamics of ECs in monolayer as a function of cell density. The results related to the dynamics of the monolayer are shown in Table 1.

3.4. Model simulates intercellular infection spread and the squeezing of infected cells prior to extrusion

After validating our *in silico* model for uninfected cell monolayers of varying cell densities, we set out to simulate the behaviour of cells in monolayer during intracellular bacterial infection with *L.m.* in an attempt to recapitulate infection spread. Prior to this, we characterised host cell kinematics and infection spread dynamics through cell monolayers *in vitro*. To that end, MDCK cells in monolayer residing on a 3 kPa gel (serving as a matrix to perform TFM [11]) were exposed to a low dosage of *L.m.* so that only sparse cells got infected across the monolayer forming distinct well-separated infection foci (domains of infected cells) over time upon *L.m.* replication and spread from one cell to another. At approximately 460 minutes post-infection (mpi), we performed time-lapse multi-channel epifluorescence microscopy imaging

Table 1
Results of the 2-D hybrid model's simulations for uninfected epithelial cell monolayers in conditions of low and high cell densities. Values represent the mean and the standard deviation. Source of the *in vitro* analysis: (1) Cellpose, (2) PIV correlation, (3) TFM, (4) MSM.

	Variable	Value			
		In silico simulation		*In vitro* experiments	
		Low density	High density	Low density	High density
Geometry	Cell area [μm^2] (1)	418.39 ± 110	175 ± 18	445.45 ± 193.66	169.62 ± 53.22
	Cell perimeter [μm] (1)	79.22 ± 9.97	50.28 ± 2.43	90.16 ± 23.47	51.81 ± 8.32
	Cell shape index [–] (1)	3.89 ± 0.1	3.79 ± 0.04	4.39 ± 0.4	4.03 ± 0.19
Kinematics	Cell displacements [μm] (1)	2.65 ± 1.48	0.55 ± 0.35	3.66 ± 2.17	0.73 ± 0.88
	Decay of the correlation coefficient of cell motion [μm^{-1}] (2)	0.023	0.0384	0.054	0.098
Dynamics	Tractions [Pa] (3)	–	–	8.74 ± 7.26	2.25 ± 1.7
	Monolayer shear stresses[Pa] (4)	40.17 ± 26.75	12.46 ± 9.64	46.69 ± 28.14	13.89 ± 8.51
	σ_I [Pa] (4)	47.36 ± 65.36	13.68 ± 22.45	46.52 ± 47.78	13.83 ± 13.03
	σ_{II} [Pa] (4)	−32.98 ± 90.78	−11.24 ± 32.98	−46.86 ± 47.94	−13.96 ± 12.65

to follow cell movement and infection spread dynamics over 1200 min (Fig. 5A, first and second row, Supplementary Video S5). We imaged: (1) the phase contrast images of cells, (2) the host cell nuclei fluorescence, (3) tracer beads' fluorescence embedded in the matrix, and (4) the *L.m.* fluorescence (Supplementary Figure S2.A).

By analysing the bacterial fluorescence images (Fig. 5A, first row) and using convex hull to find the area of infected cells per time-point [11], we monitored the growth of infection focus area overtime, and interestingly discovered that this is quasi linear, although bacterial replication is known to be exponential [6] (Fig. 5B, blue points). Subsequently, we computed the area of the infection focus and plotted it over time to derive an equation that accurately describes and explains the spread of the bacterial infection through cells. As observed in our *in vitro* experiments, *L.m.* intercellular spread approximately follows a linear law (Fig. 5B, black line). Therefore, in our model we approximated the growth of the infection focus area over time as a linear function (Fig. 5B, orange points). For the simulations we considered a high cell density monolayer ($\rho = 5708$ cells/mm^2) similar to the *in vitro* monolayers and were able to effectively recapitulate infection spread *in silico* (Fig. 5A, third row and Supplementary Video S6). To validate our *in silico* model, we measured the area of infected cells and uninfected surrounders *in vitro* and *in silico*. Consistent with previous studies, we found that infected cells pertaining in the infection focus exhibited a reduced area of 18% as compared to the surrounding uninfected cells [11]. In accordance, in our model uninfected cells at 850 mpi have an area of 175 μm^2 whereas infected cells 135 μm^2, thus are 22% smaller (Fig. 5C and Supplementary Video S7).

To determine how coordinated is the motion between neighbouring cells, and to integrate this parameter into our model, we performed PIV on the phase contrast images to calculate the correlation coefficient between neigbouring cells. We did this analysis at two different time points: (1) during early infection, when the infection focus area is still small (470 mpi); and (2) at later times, when the size of the infection focus is considerably larger (1060 mpi). We found that the correlation coefficient *in vitro* decays slower at 1060 mpi than at 470 mpi (1.73 times slower), indicating greater coordination among cells after infection mounding has started, which most likely originates from uninfected surrounder cells migrating towards the focus (Fig. 5D, left column) [11]. We then investigated whether the same tendency could be observed in our *in silico* infection experiments. Using the cell displacements of our simulation, we computed the resultant velocity field and subsequently the correlation coefficient of the cell displacement vectors. Consistent with our *in vitro* findings, in our *in silico* monolayer the decay of the correlation coefficient over distance at 1060 mpi is slower than that observed prior to the extrusion of the first cell from the monolayer (1.6 times slower) (Fig. 5D, right column). However, when compared to the *in vitro* results, the correlation coefficient in the computational model remains higher, as previously noted in uninfected monolayers.

Altogether, our current model can effectively simulate both *L.m.* infection spread through cells and recapitulate the alterations in host cell kinematics during the course of infection.

3.5. Monolayer stresses increase in uninfected cells that closely surround the infection focus in silico and in vitro

Based on our *in silico* model, an increase in coordinate movement of uninfected surrounders during infection leads to the squeezing of infected cells, similar to what happens *in vitro*. However, how cellular forces are modulated during this infection process remained obscure. To address that, we first characterised *in vitro* the forces that cells exert on their ECM and on each other (via TFM and MSM, respectively) (Fig. 6, first and second rows respectively, and Supplementary Figure S5A,B). Over the course of infection, we observed that cells pertaining the infection focus reduced the traction stresses exerted on the ECM. Conversely, the magnitude of traction stresses of uninfected surrounder cells in close proximity to the infection focus remained constant or increased during infection, as those cells actively migrated towards the infection focus (Fig. 6, first row), as previously demonstrated [11,12]. We then used the calculated traction stresses as input to approximate the inter and intra-cellular stresses through MSM [20]. We observed an increase in monolayer shear and tensile stresses at the interface between infected and uninfected cells during bacterial infection, while for infected cells the stress levels decreased (Fig. 6, second row and Supplementary Figure S5C, first row), as previously observed [12].

When we calculated the *in silico* monolayer stresses, we found that the surrounder uninfected cells in close proximity of the infection focus increased their monolayer stresses significantly at around 860 mpi, which coincides with them initiating migration towards the focus (Fig. 6, third row, Supplementary Figure S5C, second row, and Supplementary Video S8). Note that although we were not able to achieve the same magnitude of monolayer stresses *in silico* as *in vitro*, in both cases we observed an increase in monolayer shear and tensile stresses in uninfected surrounders immediately adjacent to the infection focus. A summary of the evolution of tractions and monolayer shear stresses is presented in Table 2.

4. Discussion

In this study, we have established a hybrid computational framework to simulate the shape changes, kinematics and dynamics of epithelial cells in monolayer across varying cell densities, in the absence or presence of intracellular bacterial infection, using *L.m.* as model bacterial pathogen. In the literature, diverse types of mathematical modelling approaches have been used to simulate cells in monolayers, e.g., vertex or cellular Potts models [60,61]. Although most models of epithelial cell monolayers account for the modulation of mechanical forces, they typically use either a discrete or a continuum approach [27,
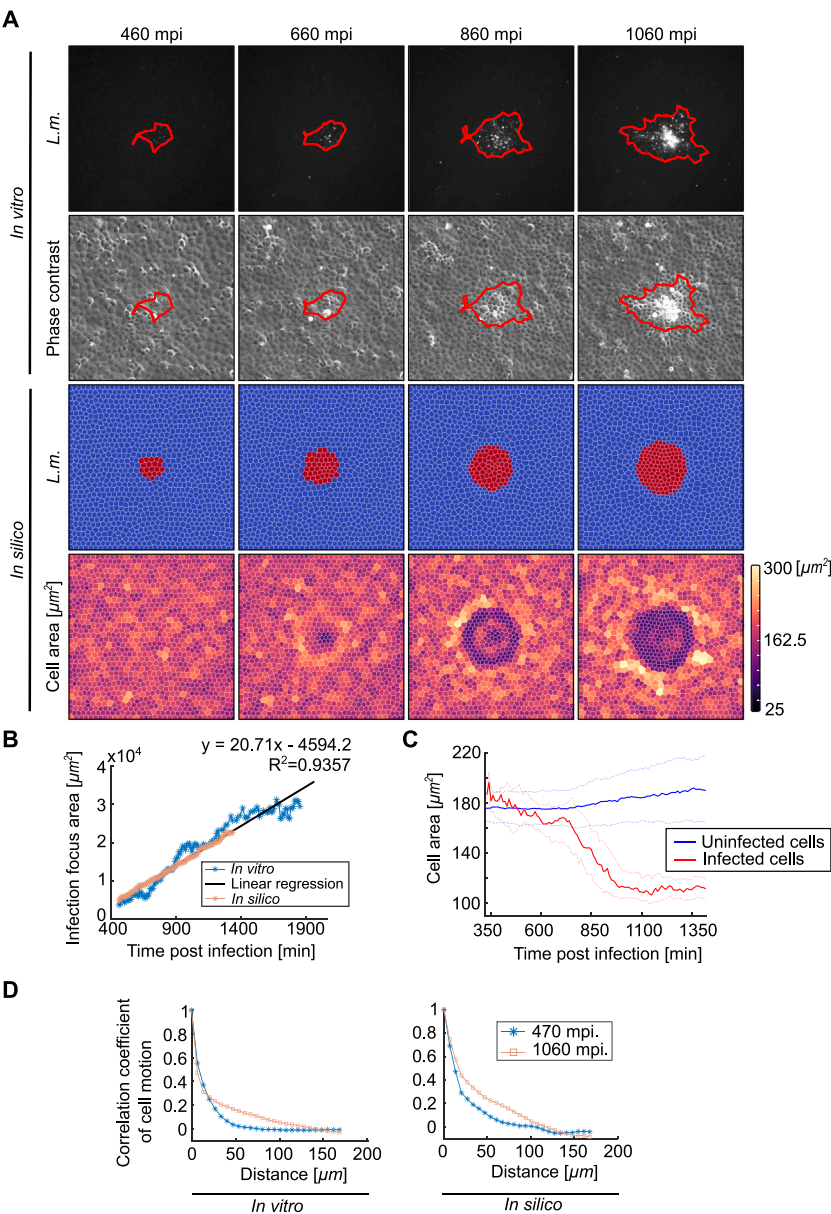
Fig. 5. *In vitro* **and** *in silico* **infection spread leads to mechanical competition between uninfected and** *L.m.* **infected cells, influencing both cell area and coordination of cell movement.** (A) Evolution of epithelial monolayers during infection (mpi: minutes post-infection). Rows include: (1) *L.m.* fluorescence microscope images (infection border in red), (2) phase contrast images of *in vitro* MDCK cells, (3) distribution of infected (in red) and uninfected (in blue) of *in silico* cells, (4) map of *in silico* cell areas. (B) Characterisation of the infection focus area over the course of the infection. (C) Evolution of average cell area in our simulations. 25th, 50th and 75th percentiles are shown. (D) Plots showing the correlation coefficient of cell displacement vectors as a function of distance in both *in vitro* (left column) and *in silico* (right column) models at two time points: 470 mpi, corresponding to a small infection focus at the beginning, and 1060 mpi, when the squeezing of infected cells becomes considerable.

Table 2
Evolution of tractions and monolayer shear stresses in *in vitro* epithelial cell monolayers infected with *L.m.* (N=3 biological replicates), along with *in silico* results from the hybrid computational model. Values represent the mean, for both infected and uninfected cell samples (mpi: minutes post infection).

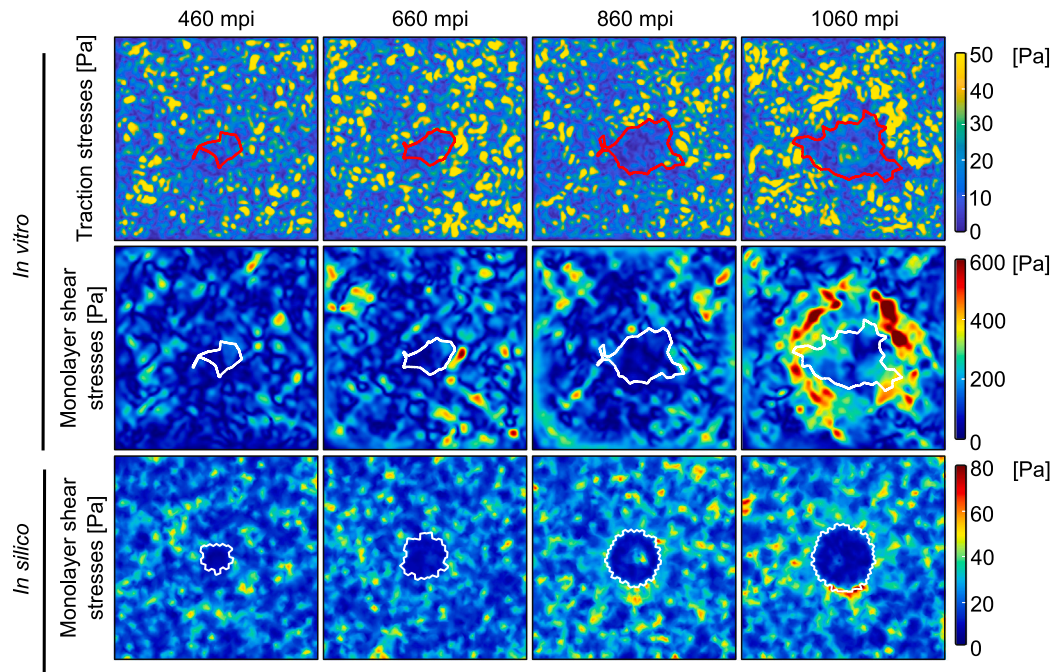|			Evolution			
			460 mpi	660 mpi	860 mpi	1060 mpi
Tractions [Pa]	*In vitro*	Infected	19.49	19.89	14.62	19.93
		Uninfected	19.34	22.87	20.57	24.07
Monolayer shear stresses [Pa]	*In vitro*	Infected	90.64	91.17	71.64	122.56
		Uninfected	102.92	122.11	116.61	153.38
	In silico	Infected	4.36	5.99	8.83	9.91
		Uninfected	14.61	15.07	17.35	17.8

Fig. 6. Uninfected cells surrounding the infection focus exhibit increased traction stresses *in vitro* and increased *in vitro* and *in silico* monolayer shear stresses during *L.m.* bacterial infection. Columns show the evolution of mechanical variables at different time points of infection (mpi: minutes post-infection). Rows display: (1) traction stresses of *in vitro* MDCK cells, (2) *in vitro* monolayer shear stresses, (3) *in silico* monolayer shear stresses. The border of the infection focus is shown in red (1st row) and white (2nd and 3rd rows).

62]. However, they fail to consider both individual cell dynamics and monolayer scale stresses. Accounting for both of these contributions is crucial for understanding what drives cell migration and maintenance of tissue continuity (i.e., barrier integrity) [18,27]. Few computational studies have considered both individual cell dynamics and changes in cell monolayer stresses, but in different contexts not involving infection. Specifically, previous hybrid models were built to investigate how cell monolayers expand through Monte Carlo simulations [63] and how epithelial cell wounds close using a 3-D continuum physics-based model [64]. Others have considered a hybrid approach to understand how epithelial cells expand and durotax but without validating the predictions with *in vitro* live-cell experimental measurements [35]. In comparison, we validated our hybrid model with *in vitro* data obtained from uninfected and infected epithelial cell monolayers.

In our hybrid model, varying cell shapes are represented as 2-D polygons using the Voronoi diagram, thus introducing and accounting for tissue heterogeneity. Voronoi tessellation has previously been used to represent cell tissue morphology in a manner that is consistent with *in vitro* cell observations [65,66]. Cell shapes are well known to depend on cell density, which in turn critically impacts the organization and motion of cells in a monolayer [48,67,68]. Previous studies have shown that the hexagonal shape and thus the number of neighbours of epithelia cells in monolayer increase with cell density [48], while the migration speed decreases since cells are constrained in motion by their neighbouring cells [17]. Consistently, using orthogonal approaches, that is our *in vitro* and *in silico* models, we found that as cell density increases, the cell shape index (measure of tissue fluidity) [69] decreases, indicating that cells get more solid-like and assume more rounded or hexagonal shapes. The CSI in the model differs slightly from that in our experiments due to how cells are represented in the model. In our experiments, cell shapes show more noise and variability than the Voronoi polygons used in the simulation, where cells exhibit regular, straight-sided shapes, while *in vitro* cell boundaries are more curved and irregular. Additionally, cell shape fluctuations are reduced at high cell densities, which also leads to decreased motility [17], as we demonstrated here. Interestingly the decrease in speed with increasing

cell density is associated with decreased coordination of motion in our hands. Although it is unclear why that occurs, it is likely that the attenuation of motility-related forces might hinder local coordination between neighbouring cells [70]. Future investigations could delve into understanding better how migration coordination is altered by physical forces and how those are modulated by cell density changes.

In our previous FEM model of epithelial cells in monolayer, for simplicity we considered idealised hexagonal cell shapes only [45]. In the model presented here, we account for cell shape heterogeneity through the epithelial monolayer, and for that purpose we had to refine our previously proposed cell protrusion and contraction laws [45]. In the current model, the degree of cell protrusion and contraction depends on the spatial distribution of the intracellular stresses and its anisotropy. This new formulation reproduces successfully the changes in cell shape, kinematics and dynamics (i.e. monolayer stresses). It is important to note that during *in silico* infection we encountered challenges in replicating the exact magnitude of monolayer stresses as during *in vitro* infection. Despite this discrepancy, cells in our model exhibited similar alterations in their monolayer stresses over the course of infection as in the *in vitro* experiments, which seems to be the crucial determinant for achieving infected cell squeezing. Our focus is on studying the alterations bacteria cause in the epithelial monolayer, rather than obtaining exactly identical stress magnitudes. Moreover, as shown in Supplementary Figure S6, there is a significant variability in monolayer stresses between replicates of infected monolayers.

The current model can simulate both the behaviour of uninfected but also of bacterially-infected epithelial cells in monolayer. In the latter case, as a model pathogen we considered *L.m.*, a facultative intracellular bacterial pathogen than can replicate intracellularly and spread from cell to cell using actin-based motility [10]. Although in our model we did not consider individual bacterial replication and spread, we did account for the fact that over the course of infection more cells get infected and thus the infection focus grows (that is the domain occupied by infected cells). This feature enabled us to simulate the course of infection over extended time periods, in contrast to our previous model, which only simulated limited cycles of cell contraction

and protrusion, since it was static (i.e., it did not account for infection spread) [12,45]. *L.m.* intercellular spread has previously been studied by Ortega et al. who used live-cell microscopy to study the dynamics of bacterial intercellular spread in epithelial cell monolayers *in vitro*. Ortega et al. mathematically modelled bacterial intercellular spread to demonstrate that *L.m.* spreads from cell to cell in a heterogeneous manner, with few bacteria displaying higher diffusion coefficients in their motion, which explains why foci are not perfect circles but instead display more heterogeneous shapes [6]. It would be interesting in a follow up study to incorporate bacterial replication and spread into our model using already available *in vitro* data of bacterial intracellular spread dynamics such as the ones provided by Ortega et al. [6]. It is also worth noting that in our current model we did not account for cell proliferation, as we maintained a fixed cell count during the simulations. Cell proliferation is an additional feature that could be incorporated into the model to examine its contribution in the outcome of the infection process.

Computational models are based on certain assumptions and therefore often present some limitations, and so does our hybrid model. One of the main limitations concerns the high number of parameters of the model and the need for their calibration. Moreover, we considered the monolayer as a 2-D structure. While it is true that the infection mounds are 3-D structures, our focus in this work was on the stages of infection prior to collective infected cell extrusion, which can be effectively described in 2-D. The 2-D modelling approach we followed is also a good approximation for comparison, considering that our *in vitro* data also consist of 2-D epifluorescence microscopy images, rather than 3-D. Future studies could implement the model in 3D by representing the cell monolayer with shell elements and incorporating the ECM, replacing the current plane stress approach, following previous work [71]. Based on cell positions in the monolayer plane, a corresponding height can be assigned vertically, determined by each particle's position from previous time steps. The outcome could be validated with new 3D microscopy data.

5. Conclusions

In summary, our novel computational approach provides a robust framework for simulating the biomechanics of epithelial cells in monolayer in the absence or presence of intracellular bacterial infection by pathogens like *L.m.* which can replicate and spread between cells. This model effectively captures changes in cell shape, kinematics and dynamics, allowing for the manipulation of parameters such as cell density and infection spread dynamics, to assess their impact on the infection process. We believe that this model is a powerful tool for understanding the complex behaviour of epithelial cells in both physiological and pathological conditions (e.g., infection), and it offers a valuable platform for future investigations, both *in vitro* and *in silico*.

CRediT authorship contribution statement

Raul Aparicio-Yuste: Writing – review & editing, Writing – original draft, Visualization, Validation, Software, Methodology, Investigation, Formal analysis, Data curation. **Lara Hundsdorfer:** Writing – review & editing, Writing – original draft, Validation, Investigation. **Effie E. Bastounis:** Writing – review & editing, Writing – original draft, Visualization, Validation, Supervision, Resources, Methodology, Investigation, Funding acquisition, Conceptualization. **Maria Jose Gomez-Benito:** Writing – review & editing, Writing – original draft, Visualization, Validation, Supervision, Software, Resources, Project administration, Methodology, Investigation, Funding acquisition, Formal analysis, Conceptualization.

Code availability

The code implemented for the hybrid model used in this study is publicly available at github.com/raparicio21/monolayer_hybrid_model.git.

Declaration of competing interest

The authors declare that they have no known competing financial interests or personal relationships that could have appeared to influence the work reported in this paper.

Appendix A. Supplementary data

Supplementary material related to this article can be found online at https://doi.org/10.1016/j.compbiomed.2024.109506.

References

[1] K.A. Jansen, D.M. Donato, H.E. Balcioglu, T. Schmidt, E.H. Danen, G.H. Koenderink, A guide to mechanobiology: Where biology and physics meet, Biochim. Biophys. Acta (BBA) 1853 (11, Part B) (2015) 3043–3052, http://dx.doi.org/10.1016/j.bbamcr.2015.05.007.

[2] P. Roca-Cusachs, V. Conte, X. Trepat, Quantifying forces in cell biology, Nature Cell Biol. 19 (7) (2017) 742–751, http://dx.doi.org/10.1038/ncb3564.

[3] L. Balasubramaniam, A. Doostmohammadi, T.B. Saw, G.H.N.S. Narayana, R. Mueller, T. Dang, M. Thomas, S. Gupta, S. Sonam, A.S. Yap, Y. Toyama, R.-M. Mège, J.M. Yeomans, B. t Ladoux, Investigating the nature of active forces in tissues reveals how contractile cells can form extensile monolayers, Nature Mater. 20 (8) (2021) 1156–1166, http://dx.doi.org/10.1038/s41563-021-00919-2.

[4] M. Luciano, S.-L. Xue, W.H.D. Vos, L. Redondo-Morata, M. Surin, F. Lafont, E. Hannezo, S. Gabriele, Cell monolayers sense curvature by exploiting active mechanics and nuclear mechanoadaptation, Nat. Phys. 17 (12) (2021) 1382–1390, http://dx.doi.org/10.1038/s41567-021-01374-1.

[5] R.L. Lamason, E. Bastounis, N.M. Kafai, R. Serrano, J.C. del Álamo, J.A. Theriot, M.D. Welch, Rickettsia Sca4 reduces vinculin-mediated intercellular tension to promote spread, Cell 167 (3) (2016) 670–683.e10, http://dx.doi.org/10.1016/j.cell.2016.09.023.

[6] F.E. Ortega, E.F. Koslover, J.A. Theriot, *Listeria monocytogenes* cell-to-cell spread in epithelia is heterogeneous and dominated by rare pioneer bacteria, eLife 8 (2019) e40032, http://dx.doi.org/10.7554/eLife.40032.

[7] C. Faralla, E.E. Bastounis, F.E. Ortega, S.H. Light, G. Rizzuto, L. Gao, D.K. Marciano, S. Nocadello, W.F. Anderson, J.R. Robbins, J.A. Theriot, A.I. Bakardjiev, Listeria monocytogenes InlP interacts with afadin and facilitates basement membrane crossing, PLOS Pathogens 14 (5) (2018) 1–26, http://dx.doi.org/10.1371/journal.ppat.1007094.

[8] T. Rajabian, B. Gavicherla, M. Heisig, S. Müller-Altrock, W. Goebel, S.D. Gray-Owen, K. Ireton, The bacterial virulence factor InlC perturbs apical cell junctions and promotes cell-to-cell spread of Listeria, Nature Cell Biol. 11 (10) (2009) 1212–1218, http://dx.doi.org/10.1038/ncb1964.

[9] A. Grassart, V. Malardé, S. Gobaa, A. Sartori-Rupp, J. Kerns, K. Karalis, B. Marteyn, P. Sansonetti, N. Sauvonnet, Bioengineered human organ-on-chip reveals intestinal microenvironment and mechanical forces impacting shigella infection, Cell Host & Microbe 26 (3) (2019) 435–444.e4, http://dx.doi.org/10.1016/j.chom.2019.08.007.

[10] E.E. Bastounis, P. Radhakrishnan, C.K. Prinz, J.A. Theriot, Mechanical forces govern interactions of host cells with intracellular bacterial pathogens, Microbiol. Mol. Biol. Rev. (2022) e0009420, http://dx.doi.org/10.1128/mmbr.00094-20.

[11] E.E. Bastounis, F. Serrano-Alcalde, P. Radhakrishnan, P. Engstrom, M.J. Gómez-Benito, M.S. Oswald, Y.-T. Yeh, J.G. Smith, M.D. Welch, J.M. García-Aznar, J.A. Theriot, Mechanical competition triggered by innate immune signaling drives the collective extrusion of bacterially infected epithelial cells, Dev. Cell 56 (4) (2021) 443–460, http://dx.doi.org/10.1016/j.devcel.2021.01.012.

[12] R. Aparicio-Yuste, M. Muenkel, A.G. Clark, M.J. Gómez-Benito, E.E. Bastounis, A stiff extracellular matrix favors the mechanical cell competition that leads to extrusion of bacterially-infected epithelial cells, Front. Cell Dev. Biol. 10 (2022) http://dx.doi.org/10.3389/fcell.2022.912318.

[13] L. Radoshevich, P. Cossart, Listeria monocytogenes: towards a complete picture of its physiology and pathogenesis, Nat. Rev. Microbiol. 16 (1) (2018) 32–46, http://dx.doi.org/10.1038/nrmicro.2017.126.

[14] J. Taelman, M. Diaz, J. Guiu, Human intestinal organoids: Promise and challenge, Front. Cell Dev. Biol. 10 (2022) http://dx.doi.org/10.3389/fcell.2022.854740.

[15] M. Ghorbaninejad, H. Asadzadeh-Aghdaei, H. Baharvand, A. Meyfour, Intestinal organoids: A versatile platform for modeling gastrointestinal diseases and monitoring epigenetic alterations, Life Sci. 319 (2023) 121506, http://dx.doi.org/10.1016/j.lfs.2023.121506.

[16] S. Henkes, K. Kostanjevec, J.M. Collinson, R. Sknepnek, E. Bertin, Dense active matter model of motion patterns in confluent cell monolayers, Nature Commun. 11 (2020) http://dx.doi.org/10.1038/s41467-020-15164-5.

[17] T.E. Angelini, E. Hannezo, X. Trepat, J.J. Fredberg, D.A. Weitz, Cell migration driven by cooperative substrate deformation patterns, Phys. Rev. Lett. 104 (2010) 168104, http://dx.doi.org/10.1103/PhysRevLett.104.168104.

[18] D.T. Tambe, C.C. Hardin, T.E. Angelini, K. Rajendran, C.Y. Park, X. Serra-Picamal, E.H. Zhou, M.H. Zaman, J.P. Butler, D.A. Weitz, J.J. Fredberg, X. Trepat, Collective cell guidance by cooperative intercellular forces, Nature Mater. 10 (6) (2011) 469–475, http://dx.doi.org/10.1038/nmat3025.

[19] D.T. Tambe, U. Croutelle, X. Trepat, C.Y. Park, J.H. Kim, E. Millet, J.P. Butler, J.J. Fredberg, Monolayer stress microscopy: Limitations, artifacts, and accuracy of recovered intercellular stresses, PLOS ONE 8 (2) (2013) 1–12, http://dx.doi.org/10.1371/journal.pone.0055172.

[20] R.A. Yuste, M. Muenkel, K. Axarlis, M.J. Gómez Benito, A. Reuss, G. Blacker, M.C. Tal, P. Kraiczy, E.E. Bastounis, Borrelia burgdorferi modulates the physical forces and immunity signaling in endothelial cells, iScience 25 (8) (2022) 104793, http://dx.doi.org/10.1016/j.isci.2022.104793.

[21] E. Balsa-Canto, A.L.-N. nez, C. Vázquez, A two-dimensional multi-species model for different Listeria monocytogenes biofilm structures and its numerical simulation, Appl. Math. Comput. 384 (2020) 125383, http://dx.doi.org/10.1016/j.amc.2020.125383.

[22] M. Delarue, J. Hartung, C. Schreck, P. Gniewek, L. Hu, S. Herminghaus, O. Hallatschek, Self-driven jamming in growing microbial populations, Nat. Phys. 12 (8) (2016) 762–766, http://dx.doi.org/10.1038/nphys3741.

[23] R. Jasevičius, R. Baronas, H. Kruggel-Emden, Numerical modelling of the normal adhesive elastic–plastic interaction of a bacterium, Adv. Powder Technol. 26 (3) (2015) 742–752, http://dx.doi.org/10.1016/j.apt.2015.04.010.

[24] M.A.A. Grant, B. Wacław, R.J. Allen, P. Cicuta, The role of mechanical forces in the planar-to-bulk transition in growing *Escherichia coli* microcolonies, J. R. Soc. Interface 11 (97) (2014) 20140400, http://dx.doi.org/10.1098/rsif.2014.0400.

[25] M. Doumic, S. Hecht, D. Peurichard, A purely mechanical model with asymmetric features for early morphogenesis of rod-shaped bacteria micro-colony, Math. Biosci. Eng. 17 (6) (2020) 6873–6908, http://dx.doi.org/10.3934/mbe.2020356.

[26] S.M. Rafelski, J.B. Alberts, G.M. Odell, An experimental and computational study of the effect of acta polarity on the speed of listeria monocytogenes actin-based motility, PLoS Comput. Biol. 5 (7) (2009) 1–14, http://dx.doi.org/10.1371/journal.pcbi.1000434.

[27] R. Alert, X. Trepat, Physical models of collective cell migration, Ann. Rev. Condens. Matter Phys. 11 (1) (2020) 77–101, http://dx.doi.org/10.1146/annurev-conmatphys-031218-013516.

[28] C.-P. Spatarelu, H. Zhang, D.T. Nguyen, X. Han, R. Liu, Q. Guo, J. Notbohm, J. Fan, L. Liu, Z. Chen, Biomechanics of collective cell migration in cancer progression: Experimental and computational methods, ACS Biomater. Sci. Eng. 5 (8) (2019) 3766–3787, http://dx.doi.org/10.1021/acsbiomaterials.8b01428.

[29] D.B. Staple, R. Farhadifar, J.-C. Röper, B. Aigouy, S. Eaton, F. Jülicher, Mechanics and remodelling of cell packings in epithelia, Eur. Phys. J. E 33 (2) (2010) 117–127, http://dx.doi.org/10.1140/epje/i2010-10677-0.

[30] A.G. Fletcher, M. Osterfield, R.E. Baker, S.Y. Shvartsman, Vertex models of epithelial morphogenesis, Biophys. J. 106 (11) (2014) 2291–2304, http://dx.doi.org/10.1016/j.bpj.2013.11.4498.

[31] P. Van Liedekerke, M.M. Palm, N. Jagiella, D. Drasdo, Simulating tissue mechanics with agent-based models: concepts, perspectives and some novel results, Comput. Part. Mech. 2 (4) (2015) 401–444, http://dx.doi.org/10.1007/s40571-015-0082-3.

[32] S. Firooz, S. Kaessmair, V. Zaburdaev, A. Javili, P. Steinmann, On continuum modeling of cell aggregation phenomena, J. Mech. Phys. Solids 167 (2022) 105004, http://dx.doi.org/10.1016/j.jmps.2022.105004.

[33] C. Falcó, D.J. Cohen, J.A. Carrillo, R.E. Baker, Quantifying tissue growth, shape and collision via continuum models and Bayesian inference, J. R. Soc. Interface 20 (204) (2023) 20230184, http://dx.doi.org/10.1098/rsif.2023.0184.

[34] M.H. Köpf, L.M. Pismen, A continuum model of epithelial spreading, Soft Matter 9 (2013) 3727–3734, http://dx.doi.org/10.1039/C3SM26955H.

[35] I. González-Valverde, J.M. García-Aznar, A hybrid computational model to explore the topological characteristics of epithelial tissues, Int. J. Numer. Methods Biomed. Eng. 33 (11) (2017) e2877, http://dx.doi.org/10.1002/cnm.2877.

[36] B.A. Camley, W.-J. Rappel, Physical models of collective cell motility: from cell to tissue, J. Phys. D: Appl. Phys. 50 (11) (2017) 113002, http://dx.doi.org/10.1088/1361-6463/aa56fe.

[37] R.C. Kennedy, G.E. Ropella, C.A. Hunt, A cell-centered, agent-based framework that enables flexible environment granularities, Theoret. Biol. Med. Model. 13 (1) (2016) 4, http://dx.doi.org/10.1186/s12976-016-0030-9.

[38] C.M. Kraning-Rush, S.P. Carey, J.P. Califano, B.N. Smith, C.A. Reinhart-King, The role of the cytoskeleton in cellular force generation in 2D and 3D environments, Phys. Biol. 8 (1) (2011) 015009, http://dx.doi.org/10.1088/1478-3975/8/1/015009.

[39] C.P. Brangwynne, F.C. MacKintosh, S. Kumar, N.A. Geisse, J. Talbot, L. Mahadevan, K.K. Parker, D.E. Ingber, D.A. Weitz, Microtubules can bear enhanced compressive loads in living cells because of lateral reinforcement , J. Cell. Biol. 173 (5) (2006) 733–741, http://dx.doi.org/10.1083/jcb.200601060.

[40] L.E. Scott, L.A. Griggs, V. Narayanan, D.E. Conway, C.A. Lemmon, S.H. Weinberg, A hybrid model of intercellular tension and cell–matrix mechanical interactions in a multicellular geometry, Biomech. Model. Mechanobiol. 19 (6) (2020) 1997–2013, http://dx.doi.org/10.1007/s10237-020-01321-8.

[41] R. Markovič, M. Marhl, M. Gosak, Mechanical cell-to-cell interactions as a regulator of topological defects in planar cell polarity patterns in epithelial tissues, Front. Mater. 7 (2020) http://dx.doi.org/10.3389/fmats.2020.00264.

[42] D. Sarkar, G. Gompper, J. Elgeti, A minimal model for structure, dynamics, and tension of monolayered cell colonies, Commun. Phys. 4 (1) (2021) 36, http://dx.doi.org/10.1038/s42005-020-00515-x.

[43] B. Rubinstein, I.M. Pinto, Epithelia migration: a spatiotemporal interplay between contraction and adhesion, Cell Adhesion & Migration 9 (5) (2015) 340–344, http://dx.doi.org/10.1080/19336918.2015.1008329.

[44] C.G. Vasquez, A.C. Martin, Force transmission in epithelial tissues, Dev. Dyn. 245 (3) (2016) 361–371, http://dx.doi.org/10.1002/dvdy.24384.

[45] R. Aparicio-Yuste, F. Serrano-Alcalde, M. Muenkel, J.M. Garcia-Aznar, E.E. Bastounis, M.J. Gomez-Benito, Computational modelling of epithelial cell monolayers during infection with listeria monocytogenes, Comput. Methods Appl. Mech. Engrg. 401 (2022) 115477, http://dx.doi.org/10.1016/j.cma.2022.115477.

[46] I. González-Valverde, J.M. García-Aznar, Mechanical modeling of collective cell migration: An agent-based and continuum material approach, Comput. Methods Appl. Mech. Engrg. 337 (2018) 246–262, http://dx.doi.org/10.1016/j.cma.2018.03.036.

[47] P. Bandil, F.J. Vernerey, Continuum theory for confluent cell monolayers: Interplay between cell growth, division, and intercalation, J. Mech. Phys. Solids 181 (2023) 105443, http://dx.doi.org/10.1016/j.jmps.2023.105443.

[48] J. Eckert, B.t Ladoux, R.-M. Mège, L. Giomi, T. Schmidt, Hexanematic crossover in epithelial monolayers depends on cell adhesion and cell density, Nature Commun. 14 (1) (2023) 5762, http://dx.doi.org/10.1038/s41467-023-41449-6.

[49] J.C. del Álamo, R. Meili, B. Alonso-Latorre, J. Rodríguez-Rodríguez, A. Aliseda, R.A. Firtel, J.C. Lasheras, Spatio-temporal analysis of eukaryotic cell motility by improved force cytometry, Proc. Natl. Acad. Sci. 104 (33) (2007) 13343–13348, http://dx.doi.org/10.1073/pnas.0705815104.

[50] E.E. Bastounis, F.E. Ortega, R. Serrano, J.A. Theriot, A multi-well format polyacrylamide-based assay for studying the effect of extracellular matrix stiffness on the bacterial infection of adherent cells, JoVE 137 (2018) e57361, http://dx.doi.org/10.3791/57361.

[51] J. Schindelin, I. Arganda-Carreras, E. Frise, V. Kaynig, M. Longair, T. Pietzsch, S. Preibisch, C. Rueden, S. Saalfeld, B. Schmid, J.-Y. Tinevez, D.J. White, V. Hartenstein, K. Eliceiri, P. Tomancak, A. Cardona, Fiji: an open-source platform for biological-image analysis, Nature Methods 9 (7) (2012) 676–682, http://dx.doi.org/10.1038/nmeth.2019.

[52] D. Ershov, M.-S. Phan, J.W. Pylvänäinen, S.U. Rigaud, L.L. Blanc, A. Charles-Orszag, J.R.W. Conway, R.F. Laine, N.H. Roy, D. Bonazzi, G. Duménil, G. Jacquemet, J.-Y. Tinevez, TrackMate 7: integrating state-of-the-art segmentation algorithms into tracking pipelines, Nature Methods 19 (7) (2022) 829–832, http://dx.doi.org/10.1038/s41592-022-01507-1.

[53] M. Pachitariu, C. Stringer, Cellpose 2.0: how to train your own model, Nature Methods 19 (12) (2022) 1634–1641, http://dx.doi.org/10.1038/s41592-022-01663-4.

[54] L. Atia, J.J. Fredberg, N.S. Gov, A.F. Pegoraro, Are cell jamming and unjamming essential in tissue development? Cells Dev. 168 (2021) 203727, http://dx.doi.org/10.1016/j.cdev.2021.203727.

[55] X. Wang, M. Merkel, L.B. Sutter, G. Erdemci-Tandogan, M.L. Manning, K.E. Kasza, Anisotropy links cell shapes to tissue flow during convergent extension, Proc. Natl. Acad. Sci. 117 (24) (2020) 13541–13551, http://dx.doi.org/10.1073/pnas.1916418117.

[56] X. Yang, D. Bi, M. Czajkowski, M. Merkel, M.L. Manning, M.C. Marchetti, Correlating cell shape and cellular stress in motile confluent tissues, Proc. Natl. Acad. Sci. 114 (48) (2017) 12663–12668, http://dx.doi.org/10.1073/pnas.1705921114.

[57] M. Sadati, A. Nourhani, J.J. Fredberg, N. Taheri Qazvini, Glass-like dynamics in the cell and in cellular collectives, WIREs Syst. Biol. Med. 6 (2) (2014) 137–149, http://dx.doi.org/10.1002/wsbm.1258.

[58] L. Gui, S.T. Wereley, A correlation-based continuous window-shift technique to reduce the peak-locking effect in digital PIV image evaluation, Exp. Fluids 32 (4) (2002) 506–517, http://dx.doi.org/10.1007/s00348-001-0396-1.

[59] A. Bajpai, J. Tong, W. Qian, Y. Peng, W. Chen, The interplay between cell-cell and cell-matrix forces regulates cell migration dynamics, Biophys. J. 117 (10) (2019) 1795–1804, http://dx.doi.org/10.1016/j.bpj.2019.10.015.

[60] P. Mosaffa, A. Rodríguez-Ferran, J.J. Muñoz, Hybrid cell-centred/vertex model for multicellular systems with equilibrium-preserving remodelling, Int. J. Numer. Methods Biomed. Eng. 34 (3) (2018) e2928, http://dx.doi.org/10.1002/cnm.2928.

[61] P.J. Albert, U.S. Schwarz, Dynamics of cell ensembles on adhesive micropatterns: Bridging the gap between single cell spreading and collective cell migration, PLoS Comput. Biol. 12 (4) (2016) 1–34, http://dx.doi.org/10.1371/journal.pcbi.1004863.

[62] S. Alt, P. Ganguly, G. Salbreux, Vertex models: from cell mechanics to tissue morphogenesis, Phil. Trans. R. Soc. B 372 (1720) (2017) 20150520, http://dx.doi.org/10.1098/rstb.2015.0520.

[63] F. Thüroff, A. Goychuk, M. Reiter, E. Frey, Bridging the gap between single-cell migration and collective dynamics, eLife 8 (2019) e46842, http://dx.doi.org/10.7554/eLife.46842.

[64] J. Bai, X. Zeng, Computational modeling and simulation of epithelial wound closure, Sci. Rep. 13 (1) (2023) 6265, http://dx.doi.org/10.1038/s41598-023-33111-4.

[65] H. Honda, Geometrical models for cells in tissues, in: G. Bourne, J. Danielli, K. Jeon (Eds.), in: International Review of Cytology, vol. 81, Academic Press, 1983, pp. 191–248, http://dx.doi.org/10.1016/S0074-7696(08)62339-6.

[66] E. Teomy, D.A. Kessler, H. Levine, Confluent and nonconfluent phases in a model of cell tissue, Phys. Rev. E 98 (2018) 042418, http://dx.doi.org/10.1103/PhysRevE.98.042418.

[67] D. Bi, J. Lopez, J.M. Schwarz, M.L. Manning, A density-independent rigidity transition in biological tissues, Nat. Phys. 11 (12) (2015) 1074–1079, http://dx.doi.org/10.1038/nphys3471.

[68] E. Lawson-Keister, M.L. Manning, Jamming and arrest of cell motion in biological tissues, Curr. Opin. Cell Biol. 72 (2021) 146–155, http://dx.doi.org/10.1016/j.ceb.2021.07.011.

[69] J.A. Mitchel, A. Das, M.J. O'Sullivan, I.T. Stancil, S.J. DeCamp, S. Koehler, O.H. Ocaña, J.P. Butler, J.J. Fredberg, M.A. Nieto, et al., In primary airway epithelial cells, the unjamming transition is distinct from the epithelial-to-mesenchymal transition, Nat. Commun. 11 (1) (2020) 5053, http://dx.doi.org/10.1038/s41467-020-18841-7.

[70] A. Loza, S. Koride, G. Schimizzi, B. Li, S. Sun, G. Longmore, Cell density and actomyosin contractility control the organization of migrating collectives within an epithelium, Mol. Biol. Cell 27 (2016) http://dx.doi.org/10.1091/mbc.E16-05-0329.

[71] R. Jakob, B.R. Britt, C. Giampietro, E. Mazza, A.E. Ehret, Discrete network models of endothelial cells and their interactions with the substrate, Biomech. Model. Mechanobiol. 23 (3) (2024) 941–957, http://dx.doi.org/10.1007/s10237-023-01815-1.